*Nano Research* 2017, 10(3): 897–907
DOI 10.1007/s12274-016-1346-9
**Research Article**

ISSN 1998-0124
CN 11-5974/O4

# Porous FeS nanofibers with numerous nanovoids obtained by Kirkendall diffusion effect for use as anode materials for sodium-ion batteries

Jung Sang Cho[1,2], Jin-Sung Park[1], and Yun Chan Kang[1] (✉)

[1] Department of Materials Science and Engineering, Korea University, Anam-Dong, Seongbuk-Gu, Seoul 136-713, Republic of Korea
[2] Department of Engineering Chemistry, Chungbuk National University, Chungbuk 361-763, Republic of Korea

**Received:** 14 August 2016
**Revised:** 18 October 2016
**Accepted:** 21 October 2016

**KEYWORDS**

iron sulfide,
sodium-ion batteries,
Kirkendall effect,
nanofibers,
electrospinning

## ABSTRACT

Porous FeS nanofibers with numerous nanovoids for use as anode materials for sodium-ion batteries were prepared by electrospinning and subsequent sulfidation. The post-treatment of the as-spun Fe(acac)$_3$-polyacrylonitrile composite nanofibers in an air atmosphere yielded hollow $Fe_2O_3$ nanofibers due to Ostwald ripening. The ultrafine $Fe_2O_3$ nanocrystals formed at the center of the fiber diffused toward the outside of the fiber via Ostwald ripening. On sulfidation, the $Fe_2O_3$ hollow nanofibers were transformed into porous FeS nanofibers, which contained numerous nanovoids. The formation of porosity in the FeS nanofibers was driven by nanoscale Kirkendall diffusion. The porous FeS nanofibers were very structurally stable and had superior sodium-ion storage properties compared with the hollow $Fe_2O_3$ nanofibers. The discharge capacities of the porous FeS nanofibers for the 1st and 150th cycles at a current density of 500 $mA \cdot g^{-1}$ were 561 and 592 $mA \cdot h \cdot g^{-1}$, respectively. The FeS nanofibers had final discharge capacities of 456, 437, 413, 394, 380, and 353 $mA \cdot h \cdot g^{-1}$ at current densities of 0.2, 0.5, 1.0, 2.0, 3.0, and 5.0 $A \cdot g^{-1}$, respectively.

## 1 Introduction

Sodium-ion batteries (SIBs) have been extensively studied as potential power sources for use in large-scale devices [1–5]. However, for many applications, the performance of SIBs must be significantly improved, for example, by developing more efficient cathode and anode materials [6–10]. Consequently, significant research efforts have been put into developing new cathode and anode materials [11–15]. Nanostructured metal sulfide materials can be synthesized by several methods and have been studied as anode materials for SIBs [16–19]. Specifically, iron sulfides (FeS and $FeS_2$) have been studied as anode materials for SIBs [20–24]. For example, Hu et al. demonstrated that $FeS_2$ microspheres, which have surprisingly high rate capabilities and an unprecedented long-term cyclability, can be used in room-temperature rechargeable sodium

---

Address correspondence to yckang@korea.ac.kr

batteries for intercalation electrochemical reactions by selecting a compatible $NaSO_3CF_3$/diglyme electrolyte and tuning the cutoff voltage to 0.8 V [20]. Lee et al. showed that FeS-reduced graphene oxide (rGO) composite powders exhibit superior sodium-ion storage performance compared with $Fe_3O_4$-rGO composite powders [21]. However, FeS nanofibers have not been studied for use as anode materials for SIBs.

Electrospinning is a simple and highly versatile method for the preparation of one-dimensional (1D) nanostructured materials of various compositions, and transition-metal oxide and sulfide nanofibers prepared by electrospinning have been used as anode materials for SIBs [6, 25–30]. Zhu et al. reported a self-standing $FeS_2$@carbon fiber cathode with $FeS_2$ nanoparticles either encapsulated in or attached to interconnected 1D carbon fibers for use in rechargeable Li–$FeS_2$ systems [31]. However, nanostructured FeS materials treated by electrospinning for use in rechargeable secondary batteries have not been studied.

In this study, porous FeS nanofibers were prepared via electrospinning and subsequent sulfidation. The $Fe_2O_3$ hollow nanofibers were transformed into porous FeS nanofibers by a simple sulfidation process. The formation of porosity in the FeS nanofibers was driven by nanoscale Kirkendall diffusion. The electrochemical properties of the porous FeS nanofibers for sodium-ion storage were compared with those of $Fe_2O_3$ hollow nanofibers.

## 2 Experimental

### 2.1 Sample preparation

Porous FeS nanofibers with numerous nanovoids were prepared in three steps: the formation of as-spun precursor nanofibers and two post-treatment steps. First, $Fe(acac)_3$-polyacrylonitrile (PAN) ($Fe(acac)_3$–PAN) composite nanofibers were prepared as precursor nanofibers by electrospinning. The precursor solution for electrospinning was prepared by dissolving $Fe(acac)_3$ (4.0 g, STREM Chemicals, 99%) and PAN (4.0 g, Aldrich, $M_W$ = 150,000) in N,N-dimethylformamide (DMF, 50 mL, Aldrich, 99%) with vigorous stirring overnight. The prepared solution was loaded at a flow rate of 2 $mL\cdot h^{-1}$ into a plastic syringe equipped with a 25-gauge stainless-steel nozzle. The solution was subsequently ejected and electrospun onto a drum collector covered with aluminum foil. During the electrospinning process, the distance between the tip and the collector and the rotation speed of the drum were set to 20 cm and 100 rpm, respectively. The applied voltage between the collector and the syringe tip was 25 kV. The resultant $Fe(acac)_3$–PAN composite nanofibers were stabilized at 200 ℃ in air for 1 h. Then, the first step in the post-treatment process was performed; the nanofibers were heated to 500 ℃ for 1 h in an air atmosphere, yielding carbon-free $Fe_2O_3$ nanofibers. In the second post-treatment step, the nanofibers were subjected to sulfidation at 400 ℃ for 8 h in $H_2S$ gas, which was generated from thiourea ($HN_2NCSNH_2$, Junsei, 98%) powder and $H_2$ gas. For the sulfidation process, the $Fe_2O_3$ nanofibers and thiourea powders were loaded into a covered alumina boat and placed in a quartz tube reactor; sulfidation resulted in the formation of porous FeS nanofibers.

### 2.2 Characterizations

The microstructures of the nanofibers were observed using scanning electron microscopy (SEM, TESCAN VEGA3 SBH) and high-resolution transmission electron microscopy (HR-TEM, JEOL JEM-2100F) at a working voltage of 200 kV. In addition, their crystal structures were examined by X-ray diffraction (XRD, X'Pert PRO MPD) using Cu $K\alpha$ radiation ($\lambda$ = 1.5418 Å) at the Korea Basic Science Institute (Daegu). X-ray photoelectron spectroscopy (XPS) was performed on the nanofibers using a Thermo Scientific K-Alpha spectrometer with Al $K\alpha$ radiation (1,486.6 eV). Thermogravimetric analysis (TGA, SDT Q600) of the nanofibers was conducted in air at a heating rate of 10 $℃\cdot min^{-1}$. The carbon-impurity content of the FeS nanofibers was determined by elemental analysis (ThermoFisher, Flash EA 2000 Series). The surface area of the nanofibers was determined using the Brunauer–Emmett–Teller (BET) method, where $N_2$ was used as the adsorbate gas.

### 2.3 Electrochemical measurements

The electrochemical properties of the nanofibers were analyzed using a 2032-type coin cell. The anode was prepared by mixing the active material—carbon black—and sodium carboxymethylcellulose at a weight ratio of 7:2:1. Sodium metal and microporous polypropylene film were used as the counter electrode and the separator, respectively. The electrolyte comprised 1 M $NaClO_4$ with 5% fluoroethylene carbonate dissolved in a mixture of ethylene carbonate and dimethyl carbonate (1:1 v/v). The discharge/charge characteristics of the samples were investigated by cycling over a potential range of 0.001 to 3 V at various current densities. Cyclic voltammograms were measured at a scan rate of 0.07 $mV\cdot s^{-1}$. The size of the negative electrode containing the nanofibers was 1.4 cm × 1.4 cm, and the mass loading was ~1.3 $mg\cdot cm^{-2}$. The electrochemical impedance was measured using electrochemical impedance spectroscopy (EIS) over a frequency range of 0.01 Hz to 100 kHz after the cell had been fully charged to 3.0 V.

## 3 Results and discussion

The formation mechanism of the porous FeS nanofibers with numerous nanovoids is illustrated in Scheme 1. The post-treatment of the as-spun $Fe(acac)_3$-PAN composite nanofibers (Scheme 1(a)) in an air atmosphere yielded hollow $Fe_2O_3$ nanofibers. The carbonization of PAN and the decomposition of $Fe(acac)_3$ yielded $Fe_3O_4$-C composite nanofibers with a filled structure, as an intermediate product (Scheme 1(b)). The combustion of carbon and oxidation of $Fe_3O_4$ produced $Fe_2O_3$ nanofibers. In this stage, Ostwald ripening resulted in the hollow $Fe_2O_3$ nanofibers (Scheme 1(c)). Ultrafine $Fe_2O_3$ nanocrystals that formed at the center of the fiber diffused toward the outside of the fiber via Ostwald ripening. Consequently, the filled-structured $Fe_3O_4$–C fibers transformed into hollow and porous $Fe_2O_3$ nanofibers. Subsequent sulfidation of the hollow $Fe_2O_3$ nanofibers at 400 °C under $H_2S$ gas produced porous structured FeS nanofibers with numerous nanovoids (Scheme 1(d)). Ultrafine nanovoids formed by nanoscale Kirkendall diffusion were uniformly distributed throughout the FeS nanofiber structure.

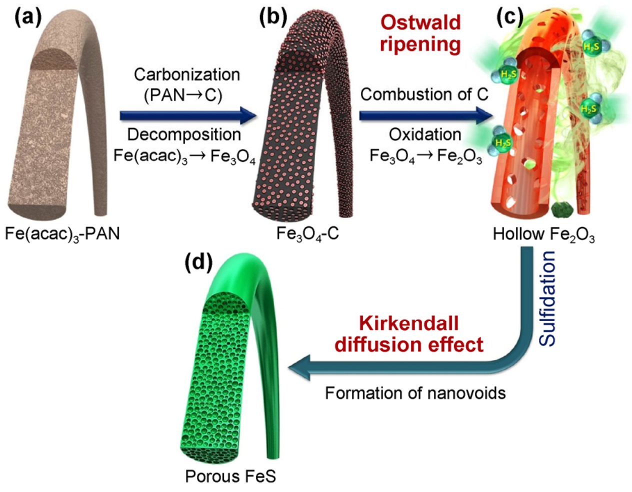

**Scheme 1** Formation mechanism of the porous FeS nanofibers with numerous nanovoids.

A detailed mechanism for the formation of nanovoids by nanoscale Kirkendall diffusion is shown in Scheme 2. The metallic Fe thin layer was first formed over the $Fe_2O_3$ nanocrystal by reduction during the sulfidation process (Schemes 2(a) and 2(b)). Fe cations with a small ionic radius ($Fe^{2+}$: 76 pm) diffused outward more quickly than $H_2S$ gas diffused inward. Accordingly, Kirkendall voids were generated near the Fe/FeS interface during vacancy-assisted exchange of the material via bulk interdiffusion (Scheme 2(c)). The reduction of $Fe_2O_3$ into Fe and the subsequent complete conversion of Fe into FeS through Kirkendall-type diffusion transformed the hollow $Fe_2O_3$ nanofibers into porous FeS nanofibers with numerous nanovoids (Scheme 2(d)).

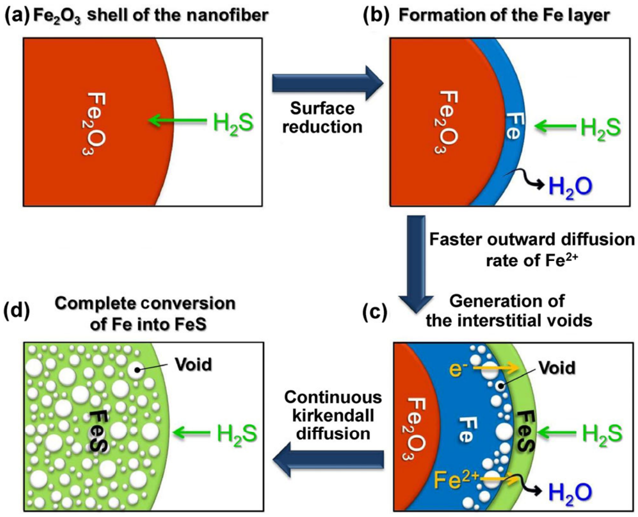

**Scheme 2** Detailed mechanism for the formation of nanovoids in the surface region of the $Fe_2O_3$ shell of the nanofibers by nanoscale Kirkendall diffusion.

The formation mechanism for the porous FeS nanofibers was investigated based on the morphological changes that occurred during the post-treatment process. The morphology and crystal structure of the stabilized electrospun nanofibers obtained by post-treatment at 200 °C under an air atmosphere are shown in Fig. S1 (in the Electronic Supplementary Material (ESM)). The nanofibers had a uniform morphology with a filled structure, as shown in Fig. S1(a) (in the ESM). Partial decomposition of Fe(acac)$_3$ during the stabilization process led to the formation of ultrafine $Fe_3O_4$ nanocrystals, as confirmed by the XRD analysis shown in Fig. S1(b) (in the ESM).

The morphologies of the $Fe_2O_3$ nanofibers formed by post-treatment of the stabilized electrospun nanofibers at 500 °C in air for 1 h are shown in Fig. 1. The SEM and TEM images shown in Figs. 1(a)–1(c) reveal the hollow and porous morphologies of the $Fe_2O_3$ nanofibers. The temperature-dependent morphological changes to the nanofibers were investigated to confirm the formation mechanism of the hollow morphologies of the $Fe_2O_3$ nanofibers. The $Fe_2O_3$-C composite nanofibers formed at 400 °C were filled, rather than being hollow, as shown in Fig. S2 (in the ESM). Therefore, the $Fe_2O_3$-C composite nanofibers with filled structure were formed as an intermediate product during the formation of the hollow $Fe_2O_3$ nanofibers at 500 °C. The filled nanofibers were transformed into the hollow $Fe_2O_3$ nanofibers by Ostwald ripening. The diameter and shell thickness of the nanofibers, as shown in Fig. 1(c), are approximately 130 and 20 nm, respectively. The HR-TEM image shown in Fig. 1(d) shows clear lattice fringes separated by 0.25 nm, corresponding to the (110) lattice plane of $Fe_2O_3$. The XRD patterns, selected-area electron diffraction (SAED) patterns, and elemental-mapping images shown in Fig. S3(a) (in the ESM), and Figs. 1(e) and 1(f), respectively, confirm the formation of carbon-free $Fe_2O_3$ nanofibers with no impurity phases after post-treatment at 500 °C.

The hollow $Fe_2O_3$ nanofibers shown in Fig. 1 were transformed into porous FeS nanofibers containing numerous nanovoids after sulfidation at 400 °C for 8 h, as shown in Fig. 2. The XRD pattern shown in Fig. S3(b) (in the ESM) indicates that the $Fe_2O_3$ was completely converted into FeS nanofibers by sulfidation. The hollow inner space of the nanofibers disappeared after sulfidation, as confirmed by inspection of the SEM and TEM images in Figs. 1 and 2, respectively. However, the ultrafine nanovoids that formed inside the FeS nanofibers remained, as shown in Figs. 2(c) and 2(d). The HR-TEM image of Fig. 2(e) shows clear lattice fringes separated by 0.27 nm, corresponding to the (112) lattice plane of FeS. The SAED pattern and elemental-mapping images shown in Figs. 2(f) and 2(g), respectively, confirm the complete transformation of $Fe_2O_3$ into FeS nanofibers by the simple sulfidation process. The $N_2$ adsorption and desorption isotherms and Barrett–Joyner–Halenda (BJH) pore-size distributions of the $Fe_2O_3$ and FeS nanofibers are shown in Fig. S4 (in the ESM). The BET surface areas of the hollow $Fe_2O_3$ and porous FeS nanofibers were 60 and

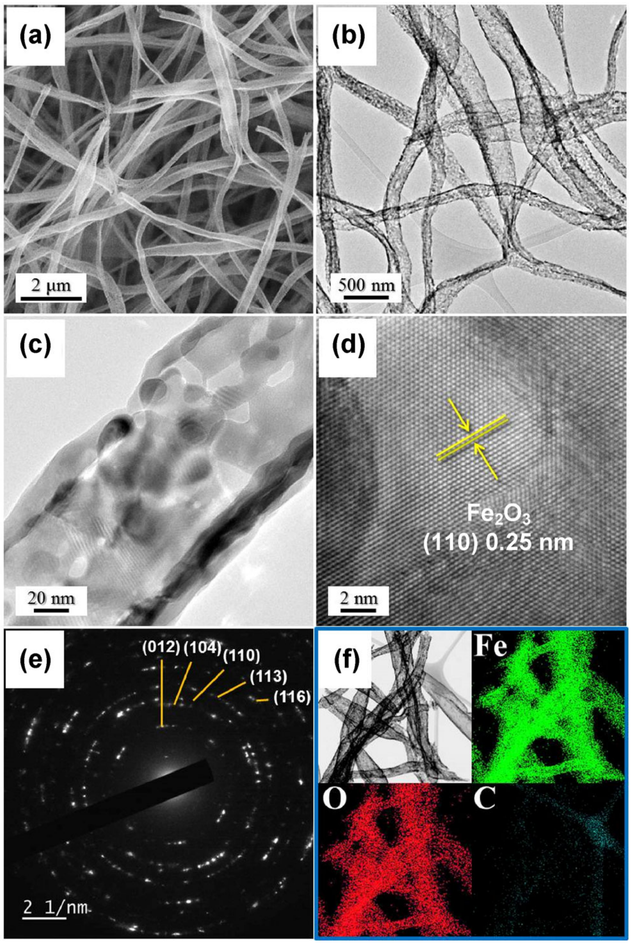

**Figure 1** Morphologies, SAED pattern, and elemental-mapping images of the $Fe_2O_3$ nanofibers after post-treatment at 500 °C for 1 h: (a) SEM image, (b) and (c) TEM images, (d) HR-TEM image, (e) SAED pattern, and (f) elemental-mapping images.

5 $m^2 \cdot g^{-1}$, respectively. The hollow $Fe_2O_3$ nanofibers exhibited well-developed mesopores between the nanocrystals. In this study, the $Fe_2O_3$ hollow nanofibers were transformed into porous FeS nanofibers, and the formation of porosity in the FeS nanofibers was driven by the nanoscale Kirkendall diffusion effect. The ultrafine nanovoids formed by nanoscale Kirkendall diffusion were mostly trapped in the dense shell structure, without gas-permeable open pores. Therefore, the porous FeS nanofibers formed by nanoscale Kirkendall diffusion had a low BET surface area compared with the hollow $Fe_2O_3$ nanofibers.

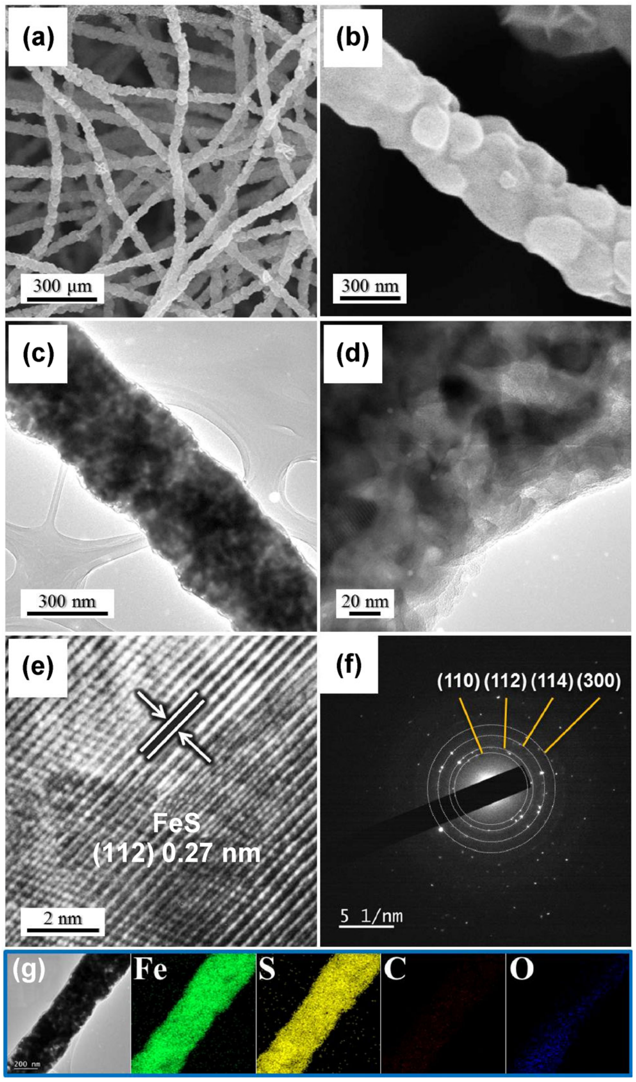

**Figure 2** Morphologies, SAED pattern, and elemental-mapping images of the porous FeS nanofibers containing numerous nanovoids after sulfidation at 400 °C for 8 h: (a) and (b) SEM images, (c) and (d) TEM images, (e) HR-TEM image, (f) SAED pattern, and (g) elemental-mapping images.

The chemical state and molecular environment of the porous FeS nanofibers were characterized by XPS. The XPS survey spectrum of the FeS nanofibers shown in Fig. 3(a) contains signals corresponding to Fe and S. In the Fe 2p spectrum of the FeS nanofibers, which is shown in Fig. 3(b), small peaks arose at binding energies of 708.4 eV for Fe $2p_{3/2}$ and 721.5 eV for Fe $2p_{1/2}$. These peaks are ascribed to $Fe^{2+}$ states in the Fe 2p spectrum of the FeS phase [21, 32, 33]. Additionally, peaks observed at binding energies of 710.6 eV for Fe $2p_{3/2}$ and 723.4 eV for Fe $2p_{1/2}$ are ascribed to $Fe^{3+}$ states that are characteristic of iron oxide ($Fe_3O_4$) [33–35]. The FeS surface was converted into iron oxide ($Fe_3O_4$) because of the high reactivity of FeS toward oxygen. In the S 2p spectrum of the porous FeS nanofibers shown in Fig. 3(c), the core-level band of the S 2p region is observed, and peaks at 161.8 and 160.8 eV, which are characteristic of FeS, correspond to S $2p_{1/2}$ and S $2p_{3/2}$, respectively [21, 32, 33]. The thermogravimetric curve of the porous FeS nanofibers shown in Fig. 3(d) reveals one-step weight gain and two-step weight loss at temperatures below 600 °C. The partial conversion reaction of FeS into $FeSO_4$ resulted in a weight increase at temperatures less than 400 °C [36–38]. The steep weight loss around 370 °C is attributed to the decomposition of FeS into $Fe_2O_3$. The final weight loss around 540 °C is attributed to the decomposition of $FeSO_4$ into $Fe_2O_3$. Carbon was not detected in the elemental analysis of the FeS nanofibers, as shown in Table S1 (in the ESM).

The sodium-ion storage performances of the porous FeS nanofibers with numerous nanovoids were compared with those of the hollow $Fe_2O_3$ nanofibers. Cyclic voltammograms (CVs) of the FeS nanofibers taken during the first seven cycles at a scan rate of 0.1 $mV \cdot s^{-1}$ in the voltage range of 0.001 to 3 V are shown in Fig. 4(a). The first cathodic scan of the FeS nanofibers contains a sharp peak at 0.77 V and a broad peak around 0.13 V. The first reduction peak at 0.77 V is attributed to the formation of $Na_xFeS$ [21, 22, 39] and the formation of a solid electrolyte interphase (SEI) by electrolyte decomposition [40]. The second broad peak at 0.13 V is attributed to the formation of Fe and $Na_2S$ [21, 22, 39]. The formation of ultrafine nanocrystals during the first cycle resulted in broad reduction peaks from the second cycle

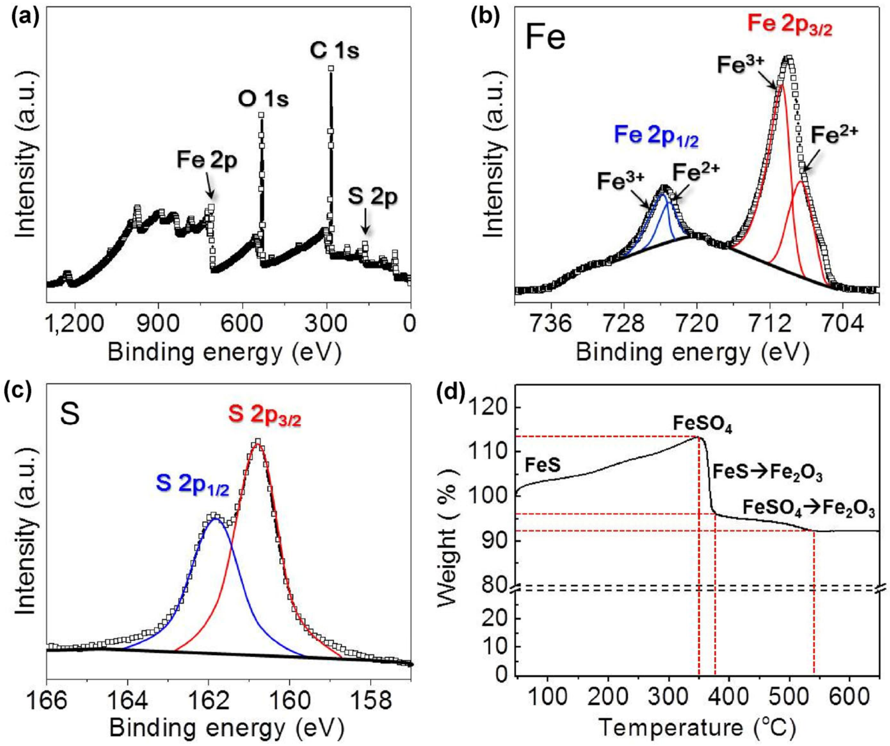

**Figure 3** XPS spectra and TGA of the porous FeS nanofibers: (a) XPS survey spectrum, (b) XPS Fe 2p spectrum, (c) XPS S 2p spectrum, and (d) TGA.

onward [41, 42]. The oxidation peaks observed at 1.41 and 1.83 V are attributed to the formation of $Na_xFeS$ and FeS, respectively [21, 22, 39]. Additionally, the small peak at 0.13 V is attributed to sodium extraction from nanopores in the FeS nanofibers [43, 44]. The charge and discharge curves of the FeS nanofibers for the 1st and 2nd cycles, which were obtained at a constant current density of 500 $mA \cdot g^{-1}$, coincide well with the CV curves. A distinct plateau around 0.77 V, due to the formation of $Na_xFeS$ and SEI by electrolyte decomposition, is observed in the first discharge curve, as shown in Fig. 4(b). However, the plateau is observed at ~0.11 V in the second discharge curve of the FeS nanofibers. The initial discharge and charge capacities of the porous FeS nanofibers were 561 and 456 $mA \cdot h \cdot g^{-1}$, respectively. In comparison, those of the hollow $Fe_2O_3$ nanofibers were 527 and 328 $mA \cdot h \cdot g^{-1}$, respectively. The initial Coulombic efficiencies of the porous FeS and hollow $Fe_2O_3$ nanofibers were 81% and 62%, respectively. The porous FeS nanofibers maintained their stable reversible discharge capacities of ~442 $mA \cdot h \cdot g^{-1}$ at a constant current density of 500 $mA \cdot g^{-1}$ during the first 30 cycles, as shown in Fig. 4(c). Then, the discharge capacities steadily increased to 592 $mA \cdot h \cdot g^{-1}$ for the remaining 120 cycles. The discharge capacities of the porous FeS nanofibers increased gradually during cycling, primarily because of the formation of a polymeric gel-like film on the active material resulting from electrolyte degradation, which has been observed in other transition metal oxides [45–47]. Generally, although the initial surface area was relatively low, after the first sodiation reaction, the FeS was converted into nano-grain metal particles in the $Na_2S$ matrix. Therefore, the surface area greatly increased. Moreover, owing to the conversion characteristic of FeS, a fresh metal surface was generated in every cathodic process. Subsequently, electrolyte decomposition occurred to form SEI films, which resulted in a gradual capacity increase [45–47]. The porous FeS nanofibers had high Coulombic efficiencies above 98% from the 3rd cycle onward. The discharge capacities of the porous FeS nanofibers and hollow $Fe_2O_3$ nanofibers for the 150th cycle were 592 and 147 $mA \cdot h \cdot g^{-1}$, respectively. The

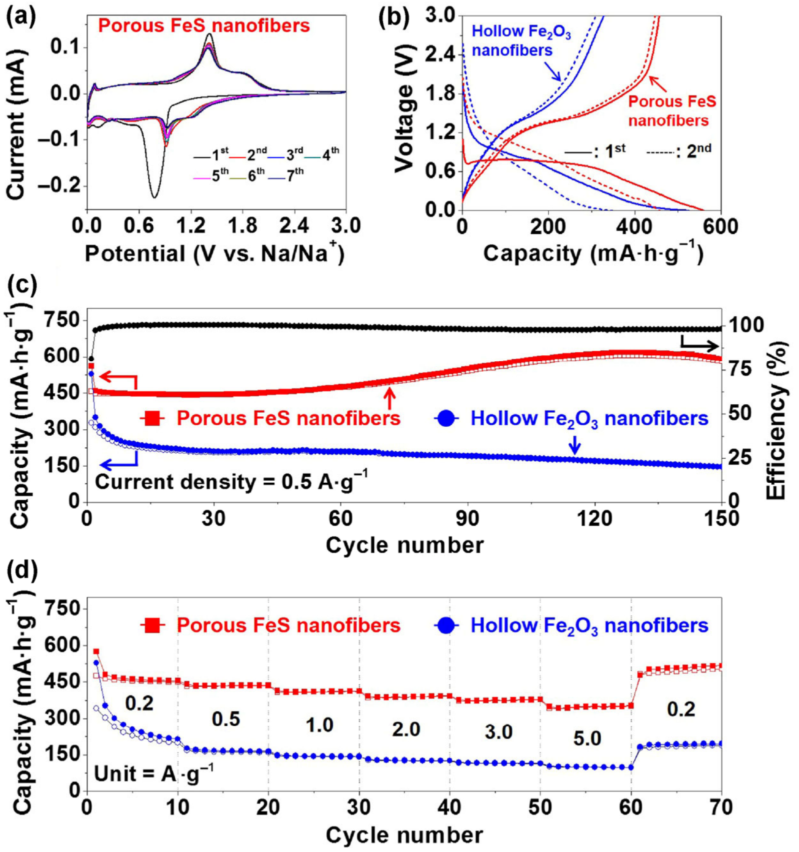

**Figure 4** Electrochemical properties of the porous FeS and hollow $Fe_2O_3$ nanofibers for sodium-ion storage: (a) CV curves for the porous FeS nanofibers, (b) 1st and 2nd charge/discharge curves at a constant current density of 500 mA·g$^{-1}$, (c) cycle performance at a constant current density of 500 mA·g$^{-1}$, and (d) rate performance at different current densities.

porous FeS nanofibers showed superior sodium-ion storage performance compared with that of the hollow $Fe_2O_3$ nanofibers. The porous FeS nanofibers had good rate performance, as shown in Fig. 4(d), in which the current density increases in a stepwise manner from 0.2 to 5.0 A·g$^{-1}$. The FeS nanofibers had final discharge capacities of 456, 437, 413, 394, 380, and 353 mA·h·g$^{-1}$ at current densities of 0.2, 0.5, 1.0, 2.0, 3.0, and 5.0 A·g$^{-1}$, respectively. In addition, the discharge capacities of the FeS nanofibers recovered well, increasing to 510 mA·h·g$^{-1}$ when the current density returned to 0.2 A·g$^{-1}$ after cycling at high current densities. On the other hand, the hollow $Fe_2O_3$ nanofibers had final discharge capacities of 214, 164, 143, 126, 115, and 97 mA·h·g$^{-1}$ at current densities of 0.2, 0.5, 1.0, 2.0, 3.0, and 5.0 A·g$^{-1}$, respectively.

The superior sodium-ion storage performance of the porous FeS nanofibers is supported by EIS analysis, as shown in Fig. 5. Nyquist plots of the porous FeS nanofibers and hollow $Fe_2O_3$ nanofibers cells before and after 1, 30, 50, and 100 cycles were obtained by deconvolution with a Randle-type equivalent-circuit model (Fig. S5(d) in the ESM) [48–50]. The equivalent-circuit model describes the electrochemical-reaction steps, including sodium-ion migration through the SEI layers, the charge-transfer reaction, and the kinetics of sodium-ion diffusion through the active material [51–53]. The medium-frequency semicircle in the Nyquist plots is attributed to the charge-transfer resistance ($R_{ct}$) between the active material and the electrolyte, and the low-frequency region corresponds to the sodium-ion diffusion process within the electrodes [54–56]. The $R_{ct}$ of the porous FeS nanofibers was 246 Ω, which is lower than that of the hollow $Fe_2O_3$ nanofibers: 429 Ω before cycling, as shown in Fig. 5(a). The ultrafine FeS nanocrystals and the high electrical conductivity of FeS compared with the $Fe_2O_3$ phase resulted in the low $R_{ct}$ of the porous FeS nanofibers

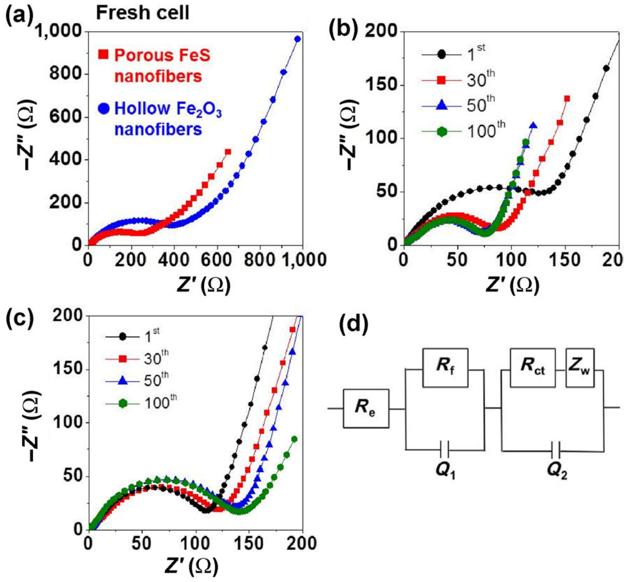

**Figure 5** Nyquist impedance plots of the porous FeS and hollow $Fe_2O_3$ nanofibers: (a) Nyquist impedance plot of the nanofibers before cycling, (b) Nyquist impedance plots of the porous FeS nanofibers after cycling, (c) Nyquist impedance plots of the hollow $Fe_2O_3$ nanofibers after cycling, and (d) equivalent-circuit model used for alternating-current impedance fitting.

[57, 58]. The $R_{ct}$ values of the porous FeS nanofibers after 1, 30, 50, and 100 cycles (shown in Fig. 5(b)) were 151, 96, 85, and 86 Ω, respectively. The formation of ultrafine FeS nanocrystals during the first cycle reduced the charge-transfer resistance. The further decrease in $R_{ct}$ over the remaining 50 cycles is attributed to the gradual activation of the porous FeS nanofibers. The $R_{ct}$ values of the hollow $Fe_2O_3$ nanofibers after 1, 30, 50, and 100 cycles, as shown in Fig. 5(c), were 119, 130, 154, and 162 Ω, respectively. The $R_{ct}$ values of the hollow $Fe_2O_3$ nanofibers increased significantly because of the structural destruction during repeated sodium-ion insertion and desertion. The results of the EIS analysis are evidence of the structural stability of the porous FeS nanofibers during the repeated sodium-ion insertion and extraction processes. The presence of nanovoids in the structure improved the structural stability of the samples.

The morphologies of the two samples obtained after 100 cycles are shown in Fig. 6. The hollow $Fe_2O_3$ nanofibers had been broken into several pieces after cycling (Fig. 6(a)). The large volume change during the repeated sodium insertion and desertion destroyed the fiber morphology. However, the overall morphology of the porous FeS nanofibers was maintained, even after 100 cycles at a current density of 500 mA·g$^{-1}$ (Fig. 6(b)). The numerous nanovoids in the FeS nanofibers accommodated the large volume change due

**(a) Hollow $Fe_2O_3$ nanofibers**

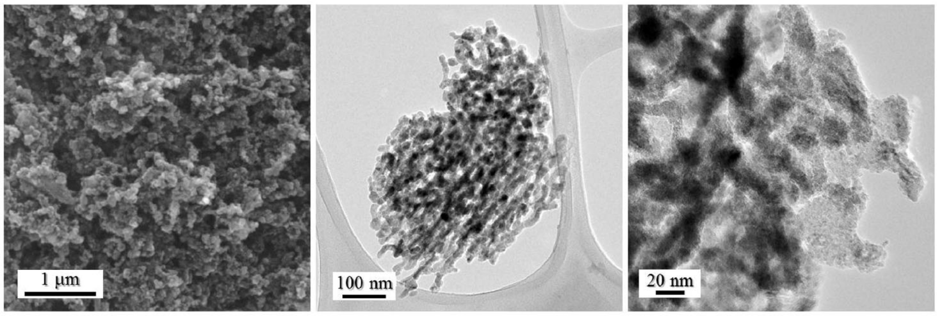

**(b) Porous FeS nanofibers**

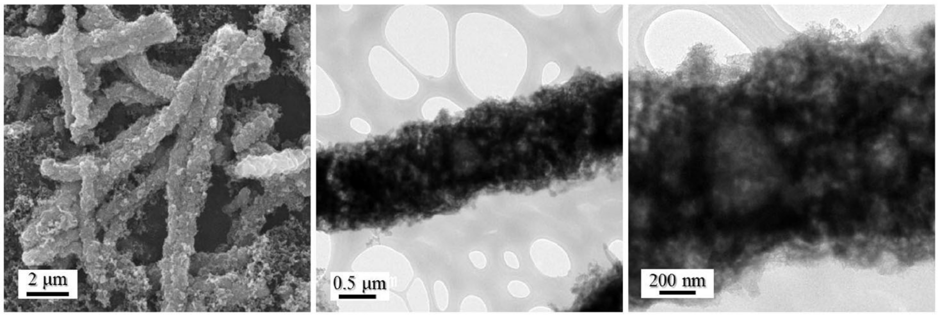

**Figure 6** Morphologies of (a) hollow $Fe_2O_3$ nanofibers and (b) porous FeS nanofibers after 100 cycles.

to the repeated sodium insertion and desertion. In summary, the porous FeS nanofibers were highly structurally stable and had superior sodium-ion storage properties compared with hollow $Fe_2O_3$ nanofibers.

The electrochemical properties of the iron-sulphide anodes for sodium-ion batteries reported thus far and the electrochemical properties of the iron are summarized in Table S2 (in the ESM). In this study, the porous FeS nanofibers with numerous nanovoids showed superior electrochemical properties for sodium-ion storage compared with iron-sulphide materials reported in the literature. This is because the porous FeS nanofibers have high structural stability during repeated sodium insertion and desertion.

## 4 Conclusions

Porous FeS nanofibers prepared by a simple two-step post-treatment process were studied for use as anode materials for sodium-ion batteries. The first post-treatment step of the electrospun nanofibers was to heat the fibers in an air atmosphere, producing carbon-free, hollow $Fe_2O_3$ nanofibers by Ostwald ripening. In the second step, the hollow $Fe_2O_3$ nanofibers were sulfidated in $H_2S$ gas, forming porous FeS nanofibers with numerous nanovoids. The Kirkendall effect played a key role in the formation of the porous FeS nanofibers. The porous FeS nanofibers were very structurally stable and had superior sodium-ion storage properties compared with the hollow $Fe_2O_3$ nanofibers. The simple fabrication process introduced in this study can be applied to the preparation of transition-metal sulfide nanofibers with various compositions for wide applications, including energy storage.

## Acknowledgements

This work was supported by a National Research Foundation of Korea (NRF) grant funded by the Korea government (MEST) (No. NRF-2015R1A2A1A15056049). This work was supported by the Energy Efficiency & Resources Core Technology Program of the Korea Institute of Energy Technology Evaluation and Planning (KETEP), granted financial resource from the Ministry of Trade, Industry & Energy, Republic of Korea (No. 20153030091450).

**Electronic Supplementary Material**: Supplementary material (morphologies and phase analysis of the $Fe_3O_4$-carbon composite nanofibers and $Fe_xO_y$-carbon composite nanofibers, XRD patterns of the nanofibers, $N_2$ adsorption–desorption isotherms and BJH adsorption pore size distribution for the FeS nanofibers, and CV curves of the hollow $Fe_2O_3$ nanofibers) is available in the online version of this article at http://dx.doi.org/10.1007/s12274-016-1346-9.

## References

[1] Hong, S. Y.; Kim, Y.; Park, Y.; Choi, A.; Choi, N.-S.; Lee, K. T. Charge carriers in rechargeable batteries: Na ions vs. Li ions. *Energy Environ. Sci.* **2013**, *6*, 2067–2081.

[2] Kim, S. W.; Seo, D. H.; Ma, X. H.; Ceder, G.; Kang, K. Electrode materials for rechargeable sodium-ion batteries: Potential alternatives to current lithium-ion batteries. *Adv. Energy Mater.* **2012**, *2*, 710–721.

[3] Palomares, V.; Serras, P.; Villaluenga, I.; Hueso, K. B.; Carretero-González, J.; Rojo, T. Na-ion batteries, recent advances and present challenges to become low cost energy storage systems. *Energy Environ. Sci.* **2012**, *5*, 5884–5901.

[4] Slater, M. D.; Kim, D.; Lee, E.; Johnson, C. S. Sodium-ion batteries. *Adv. Funct. Mater.* **2013**, *23*, 947–958.

[5] You, Y.; Wu, X.-L.; Yin, Y.-X.; Guo, Y.-G. High-quality prussian blue crystals as superior cathode materials for room-temperature sodium-ion batteries. *Energy Environ. Sci.* **2014**, *7*, 1643–1647.

[6] Cho, J. S.; Lee, S. Y.; Kang, Y. C. First introduction of $NiSe_2$ to anode material for sodium-ion batteries: A hybrid of graphene-wrapped $NiSe_2$/C porous nanofiber. *Sci. Rep.* **2016**, *6*, 23338.

[7] Zhang, Z.; Shi, X. D.; Yang, X.; Fu, Y.; Zhang, K.; Lai, Y. Q.; Li, J. Nanooctahedra particles assembled $FeSe_2$ microspheres embedded into sulfur-doped reduced graphene oxide sheets as a promising anode for sodium ion batteries. *ACS Appl. Mater. Interfaces* **2016**, *8*, 13849–13856.

[8] Qian, J. F.; Xiong, Y.; Cao, Y. L.; Ai, X. P.; Yang, H. X. Synergistic Na-storage reactions in $Sn_4P_3$ as a high-capacity, cycle-stable anode of Na-ion batteries. *Nano Lett.* **2014**, *14*, 1865–1869.

[9] Wang, L.; Lu, Y. H.; Liu, J.; Xu, M. W.; Cheng, J. G.; Zhang, D. W.; Goodenough, J. B. A superior low-cost cathode for a Na-ion battery. *Angew. Chem., Int. Ed.* **2013**, *52*, 1964–1967.

[10] You, Y.; Yu, X. Q.; Yin, Y. X.; Nam, K.-W.; Guo, Y.-G. Sodium iron hexacyanoferrate with high Na content as a

Na-rich cathode material for Na-ion batteries. *Nano Res.* **2015**, *8*, 117–128.

[11] Cho, J. S.; Won, J. M.; Lee, J.-K.; Kang, Y. C. Design and synthesis of multiroom-structured metal compounds–carbon hybrid microspheres as anode materials for rechargeable batteries. *Nano Energy* **2016**, *26*, 466–478.

[12] Dong, Y. F.; Li, S.; Zhao, K. N.; Han, C. H.; Chen, W.; Wang, B. L.; Wang, L.; Xu, B. A.; Wei, Q. L.; Zhang, L. et al. Hierarchical zigzag $Na_{1.25}V_3O_8$ nanowires with topotactically encoded superior performance for sodium-ion battery cathodes. *Energy Environ. Sci.* **2015**, *8*, 1267–1275.

[13] Li, S.; Dong, Y. F.; Xu, L.; Xu, X.; He, L.; Mai, L. Q. Effect of carbon matrix dimensions on the electrochemical properties of $Na_3V_2(PO_4)_3$ nanograins for high-performance symmetric sodium-ion batteries. *Adv. Mater.* **2014**, *26*, 3545–3553.

[14] Gu, X.; Li, L. J.; Wang, Y.; Dai, P. C.; Wang, H. B.; Zhao, X. B. Hierarchical tubular structures constructed from rutile $TiO_2$ nanorods with superior sodium storage properties. *Electrochim. Acta* **2016**, *211*, 77–82.

[15] Liu, J.; Kopold, P.; Wu, C.; van Aken, P. A.; Maier, J.; Yu, Y. Uniform yolk–shell $Sn_4P_3$@C nanospheres as high-capacity and cycle-stable anode materials for sodium-ion batteries. *Energy Environ. Sci.* **2015**, *8*, 3531–3538.

[16] Yu, D. Y. W.; Prikhodchenko, P. V.; Mason, C. W.; Batabyal, S. K.; Gun, J.; Sladkevich, S.; Medvedev, A. G.; Lev, O. High-capacity antimony sulphide nanoparticle-decorated graphene composite as anode for sodium-ion batteries. *Nat. Commun.* **2013**, *4*, 2922.

[17] Hu, Z.; Wang, L. X.; Zhang, K.; Wang, J. B.; Cheng, F. Y.; Tao, Z. L.; Chen, J. $MoS_2$ nanoflowers with expanded interlayers as high-performance anodes for sodium-ion batteries. *Angew. Chem., Int. Ed.* **2014**, *126*, 13008–13012.

[18] Lacey, S. D.; Wan, J. Y.; Cresce, A. v. W.; Russell, S. M.; Dai, J. Q.; Bao, W. Z.; Xu, K.; Hu, L. B. Atomic force microscopy studies on molybdenum disulfide flakes as sodium-ion anodes. *Nano Lett.* **2015**, *15*, 1018–1024.

[19] Peng, S. J.; Han, X. P.; Li, L. L.; Zhu, Z. Q.; Cheng, F. Y.; Srinivansan, M.; Adams, S.; Ramakrishna, S. Unique cobalt sulfide/reduced graphene oxide composite as an anode for sodium-ion batteries with superior rate capability and long cycling stability. *Small* **2016**, *12*, 1359–1368.

[20] Hu, Z.; Zhu, Z. Q.; Cheng, F. Y.; Zhang, K.; Wang, J. B.; Chen, C. C.; Chen, J. Pyrite $FeS_2$ for high-rate and long-life rechargeable sodium batteries. *Energy Environ. Sci.* **2015**, *8*, 1309–1316.

[21] Lee, S. Y.; Kang, Y. C. Sodium-ion storage properties of FeS–reduced graphene oxide composite powder with a crumpled structure. *Chem.—Eur. J.* **2016**, *22*, 2769–2774.

[22] Walter, M.; Zünd, T.; Kovalenko, M. V. Pyrite ($FeS_2$) nanocrystals as inexpensive high-performance lithium-ion cathode and sodium-ion anode materials. *Nanoscale* **2015**, *7*, 9158–9163.

[23] Zhang, S. S. The redox mechanism of $FeS_2$ in non-aqueous electrolytes for lithium and sodium batteries. *J. Mater. Chem. A* **2015**, *3*, 7689–7694.

[24] Zhu, Y. J.; Suo, L. M.; Gao, T.; Fan, X. L.; Han, F. D.; Wang, C. S. Ether-based electrolyte enabled Na/$FeS_2$ rechargeable batteries. *Electrochem. Commun.* **2015**, *54*, 18–22.

[25] Dirican, M.; Lu, Y.; Ge, Y. Q.; Yildiz, O.; Zhang, X. W. Carbon-confined $SnO_2$-electrodeposited porous carbon nanofiber composite as high-capacity sodium-ion battery anode material. *ACS Appl. Mater. Interfaces* **2015**, *7*, 18387–18396.

[26] Liu, Y. C.; Zhang, N.; Yu, C. M.; Jiao, L. F.; Chen, J. $MnFe_2O_4$@C nanofibers as high-performance anode for sodium-ion batteries. *Nano Lett.* **2016**, *16*, 3321–3328.

[27] Niu, C. J.; Meng, J. S.; Wang, X. P.; Han, C. H.; Yan, M. Y.; Zhao, K. N.; Xu, X. M.; Ren, W. H.; Zhao, Y. L.; Xu, L. et al. General synthesis of complex nanotubes by gradient electrospinning and controlled pyrolysis. *Nat. Commun.* **2015**, *6*, 7402.

[28] Wang, X. Y.; Fan, L.; Gong, D. C.; Zhu, J.; Zhang, Q. F.; Lu, B. G. Core–shell Ge@graphene@$TiO_2$ nanofibers as a high-capacity and cycle-stable anode for lithium and sodium ion battery. *Adv. Funct. Mater.* **2016**, *26*, 1104–1111.

[29] Xiong, Y.; Qian, J. F.; Cao, Y. L.; Ai, X. P.; Yang, H. X. Electrospun $TiO_2$/C nanofibers as a high-capacity and cycle-stable anode for sodium-ion batteries. *ACS Appl. Mater. Interfaces* **2016**, *8*, 16684–16689.

[30] Cho, J. S.; Lee, J.-K.; Kang, Y. C. Graphitic carbon-coated $FeSe_2$ hollow nanosphere-decorated reduced graphene oxide hybrid nanofibers as an efficient anode material for sodium ion batteries. *Sci. Rep.* **2016**, *6*, 23699.

[31] Zhu, Y.; Fan, X.; Suo, L.; Luo, C.; Gao, T.; Wang, C. Electrospun $FeS_2$@carbon fiber electrode as a high energy density cathode for rechargeable lithium batteries. *ACS Nano* **2016**, *10*, 1529–1538.

[32] Wang, M. D.; Xue, D. P.; Qin, H. Y.; Zhang, L.; Ling, G. P.; Liu, J. B.; Fang, Y. T.; Meng, L. Preparation of $FeS_2$ nanotube arrays based on layer-by-layer assembly and their photoelectrochemical properties. *Mater. Sci. Eng. B* **2016**, *204*, 38–44.

[33] Shao, D. D.; Wang, X. X.; Li, J. X.; Huang, Y. S.; Ren, X. M.; Hou, G. S.; Wang, X. K. Reductive immobilization of uranium by PAAM–FeS/$Fe_3O_4$ magnetic composites. *Environ. Sci.: Water Res. Technol.* **2015**, *1*, 169–176.

[34] Han, F.; Ma, L. J.; Sun, Q.; Lei, C.; Lu, A. H. Rationally designed carbon-coated $Fe_3O_4$ coaxial nanotubes with

hierarchical porosity as high-rate anodes for lithium ion batteries. *Nano Res.* **2014**, *7*, 1706–1717.

[35] Luo, J. S.; Liu, J. L.; Zeng, Z. Y.; Ng, C. F.; Ma, L. J.; Zhang, H.; Lin, J. Y.; Shen, Z. X.; Fan, H. J. Three-dimensional graphene foam supported $Fe_3O_4$ lithium battery anodes with long cycle life and high rate capability. *Nano Lett.* **2013**, *13*, 6136–6143.

[36] Kennedy, T.; Sturman, B. T. The oxidation of iron (II) sulphide. *J. Therm. Anal.* **1975**, *8*, 329–337.

[37] Schwab, G. M.; Philinis, J. Reactions of iron pyrite: Its thermal decomposition, reduction by hydrogen and air oxidation. *J. Am. Chem. Soc.* **1947**, *69*, 2588–2596.

[38] Coombs, P. G.; Munir, Z. A. The mechanism of oxidation of ferrous sulfide (FeS) powders in the range of 648 to 923 K. *Metall. Trans. B* **1989**, *20*, 661–670.

[39] Wang, Y.-X.; Yang, J. P.; Chou, S.-L.; Liu, H. K.; Zhang, W.-X.; Zhao, D. Y.; Dou, S. X. Uniform yolk–shell iron sulfide-carbon nanospheres for superior sodium-iron sulfide batteries. *Nat. Commun.* **2015**, *6*, 8689.

[40] Cao, Y. L.; Xiao, L. F.; Sushko, M. L.; Wang, W.; Schwenzer, B.; Xiao, J.; Nie, Z. M.; Saraf, L. V.; Yang, Z. G.; Liu, J. Sodium ion insertion in hollow carbon nanowires for battery applications. *Nano Lett.* **2012**, *12*, 3783–3787.

[41] Cho, J. S.; Won, J. M.; Lee, J.-H.; Kang, Y. C. Synthesis and electrochemical properties of spherical and hollow-structured NiO aggregates created by combining the Kirkendall effect and Ostwald ripening. *Nanoscale* **2015**, *7*, 19620–19626.

[42] Sun, Y. M.; Hu, X. L.; Luo, W.; Xia, F. F.; Huang, Y. H. Reconstruction of conformal nanoscale MnO on graphene as a high-capacity and long-life anode material for lithium ion batteries. *Adv. Funct. Mater.* **2013**, *23*, 2436–2444.

[43] Tang, K.; Fu, L. J.; White, R. J.; Yu, L. H.; Titirici, M. M.; Antonietti, M.; Maier, J. Hollow carbon nanospheres with superior rate capability for sodium-based batteries. *Adv. Energy Mater.* **2012**, *2*, 873–877.

[44] Douglas, A.; Carter, R.; Oakes, L.; Share, K.; Cohn, A. P.; Pint, C. L. Ultrafine iron pyrite ($FeS_2$) nanocrystals improve sodium–sulfur and lithium–sulfur conversion reactions for efficient batteries. *ACS Nano* **2015**, *9*, 11156–11165.

[45] Bai, J.; Li, X. G.; Liu, G. Z.; Qian, Y. T.; Xiong, S. L. Unusual formation of $ZnCo_2O_4$ 3D hierarchical twin microspheres as a high-rate and ultralong-life lithium-ion battery anode material. *Adv. Funct. Mater.* **2014**, *24*, 3012–3020.

[46] Su, L. W.; Zhong, Y. R.; Zhou, Z. Role of transition metal nanoparticles in the extra lithium storage capacity of transition metal oxides: A case study of hierarchical core–shell $Fe_3O_4$@C and Fe@C microspheres. *J. Mater. Chem. A* **2013**, *1*, 15158–15166.

[47] Zhou, L.; Zhao, D. Y.; Lou, X. W. Double-shelled $CoMn_2O_4$ hollow microcubes as high-capacity anodes for lithium-ion batteries. *Adv. Mater.* **2012**, *24*, 745–748.

[48] Cho, J. S.; Hong, Y. J.; Lee, J.-H.; Kang, Y. C. Design and synthesis of micron-sized spherical aggregates composed of hollow $Fe_2O_3$ nanospheres for use in lithium-ion batteries. *Nanoscale* **2015**, *7*, 8361–8367.

[49] Cho, J. S.; Kang, Y. C. Nanofibers comprising yolk–shell Sn@void@$SnO/SnO_2$ and hollow $SnO/SnO_2$ and $SnO_2$ nanospheres via the Kirkendall diffusion effect and their electrochemical properties. *Small* **2015**, *11*, 4673–4681.

[50] Ngo, D. T.; Kalubarme, R. S.; Le, H. T. T.; Fisher, J. G.; Park, C. N.; Kim, I. D.; Park, C. J. Carbon-interconnected Ge nanocrystals as an anode with ultra-long-term cyclability for lithium ion batteries. *Adv. Funct. Mater.* **2014**, *24*, 5291–5298.

[51] Wu, H.; Xu, M.; Wang, Y. C.; Zheng, G. F. Branched $Co_3O_4/Fe_2O_3$ nanowires as high capacity lithium-ion battery anodes. *Nano Res.* **2013**, *6*, 167–173.

[52] Wu, H.; Xu, M.; Wu, H. Y.; Xu, J. J.; Wang, Y. L.; Peng, Z.; Zheng, G. F. Aligned NiO nanoflake arrays grown on copper as high capacity lithium-ion battery anodes. *J. Mater. Chem.* **2012**, *22*, 19821–19825.

[53] Liu, Y. J.; Li, X. H.; Guo, H. J.; Wang, Z. X.; Hu, Q. Y.; Peng, W. J.; Yang, Y. Electrochemical performance and capacity fading reason of $LiMn_2O_4$/graphite batteries stored at room temperature. *J. Power Sources* **2009**, *189*, 721–725.

[54] Cho, J. S.; Hong, Y. J.; Kang, Y. C. Design and synthesis of bubble-nanorod-structured $Fe_2O_3$–carbon nanofibers as advanced anode material for Li-ion batteries. *ACS Nano* **2015**, *9*, 4026–4035.

[55] Wang, Z. Y.; Luan, D. Y.; Madhavi, S.; Hu, Y.; Lou, X. W. D. Assembling carbon-coated $\alpha$-$Fe_2O_3$ hollow nanohorns on the CNT backbone for superior lithium storage capability. *Energy Environ. Sci.* **2012**, *5*, 5252–5256.

[56] Xu, Y. H.; Zhu, Y. J.; Liu, Y. H.; Wang, C. S. Electrochemical performance of porous carbon/tin composite anodes for sodium-ion and lithium-ion batteries. *Adv. Energy Mater.* **2013**, *3*, 128–133.

[57] Mussatti, E.; Merlini, C.; Barra, G. M. D. O.; Güths, S.; de Oliveira, A. P. N.; Siligardi, C. Evaluation of the properties of iron oxide-filled castor oil polyurethane. *Mater. Res.* **2013**, *16*, 65–70.

[58] Zeng, S. L.; Wang, H. X.; Dong, C. Synthesis and electrical conductivity of nanocrystalline tetragonal FeS. *Chinese Phys. B* **2014**, *23*, 087203.